Induction Infrared Thermography and Thermal-Wave-Radar Analysis for Imaging Inspection and Diagnosis of Blade Composites

Ruizhen Yang, *Member, IEEE*, Yunze He, *Member, IEEE*, Andreas Mandelis, Nichen Wang, Xuan Wu, and Shoudao Huang, *Senior Member, IEEE*

***Abstract*—Condition monitoring, nondestructive testing, and fault diagnosis are currently considered crucial processes for on-condition maintenance (OCM) to increase the reliability and availability of wind turbines and reduce the wind energy generation cost. Carbon fiber reinforced plastics (CFRPs) have been increasingly used to fabricate wind turbine blades. Delamination-type damage is inevitable during manufacture or in-service of a CFRP blade. This inner (subsurface) flaw, usually difficult to be detected by artificial visual inspection or machine vision based on CCD or CMOS, severely degrades the load-bearing capacity of a blade. Induction infrared thermography (IIT) is an emerging infrared machine vision inspection technology, which has the capability of insight to CFRP based on electromagnetic induction and heat conduction. This paper introduces photothermal thermal-wave radar (TWR) nondestructive imaging (NDI) to IIT, based on cross-correlation (CC) pulse compression and matched filtering and applies TWR principles to CFRP imaging inspection and diagnosis. The experimental studies carried out under the transmission mode have shown that TWR B-scan and phasegram can be used to inspect and diagnose subsurface delaminations in CFRP with improved signal-to-noise ratio (SNR) and shape identification. As a new machine vision inspection method, TWRI will play an important role in the OCM of the wind turbine blade.**

***Index Terms*—Blade, diagnosis, imaging inspection, induction infrared thermography, machine vision, nondestructive infrared imaging, on-condition maintenance, thermographic analysis, Thermal-Wave Radar NDI, wind turbine.**

Manuscript received March 5, 2018; revised April 15, 2018; accepted May 3, 2018. Date of publication May 8, 2018; date of current version December 3, 2018. This work was supported in part by the National Key Research and Development Program of China under Grant 2016YFF0203400, in part by the National Natural Science Foundation of China under Grant 61501483 and 51408071, and in part by the China Postdoctoral Science Foundation Funded Project under Grant 2017M612549 and Grant 2017T100598, and in part by the Natural Sciences and Engineering Research Council of Canada (NSERC) Discovery Grants Program and the NSERC – Collaborative Research and Training Experience (CREATE). The work of A. Mandelis was supported by the NSERC Discovery grant and the NSERC – Collaborative Research and Training Experience (CREATE) Program. Paper no. TII-18-0594. *(Corresponding author: Yunze He.)*

R. Yang is with the College of Civil Engineering, Changsha University, Changsha 410022, China, and also with the College of Electrical and Information Engineering, Hunan University, Changsha 410082, China (e-mail: xbaiyang@163.com).

Y. He is with the College of Electrical and Information Engineering, Hunan University, Changsha 410082, China, and also with the Fujian Province University Key Laboratory of Nondestructive Testing, Fuqing Branch of Fujian Normal University, Fuzhou 350300, China (e-mail: hejicker@163.com).

A. Mandelis is with the Center for Advanced Diffusion-Wave and Photoacoustic Technologies (CADIFT), MIE, University of Toronto, Toronto, ON M5S 1A1, Canada, and also with the University of Electronic Science and Technology of China, Chengdu, 610054, China (e-mail: mandelis@mie.utoronto.ca).

N. Wang, X. Wu, and S. Huang are with the College of Electrical and Information Engineering, Hunan University, Changsha 410082, China (e-mail: wncvip@qq.com; wuxuan24@163.com; shoudaohuang@tom.com).

Color versions of one or more of the figures in this paper are available online at http://ieeexplore.ieee.org.

Digital Object Identifier 10.1109/TII.2018.2834462

Nomenclature

CC	Cross correlation.
CDT	Cross-delay time.
CFRP	Carbon-fiber-reinforced plastics.
CM	Condition monitoring.
DL	Digital level.
ECPPT	Eddy current pulsed phase thermography.
ECPT	Eddy current pulsed thermography.
EMI	Electromagnetic induction.
FWS	Fiber-woven structures.
IIT	Induction infrared thermography.
IR	Infrared.
MUT	Material under testing.
NDI	Nondestructive imaging.
NDT	Nondestructive testing.
NHE	Nonuniform heating effect.
O&M	Operational and maintenance.
OCM	On-condition maintenance.
SNR	Signal-to-noise ratio.
TAR	Thermal accumulation region.
TC-PCT	Truncated-correlation photothermal coherence tomography.
TDR	Thermal depletion region.
TWR(I)	Thermal wave radar (imaging).
VH	Volumetric heating.
WT	Wind turbine.

I. Introduction

WIND turbines (WTs) have become a key system with wind energy be important composition of renewable

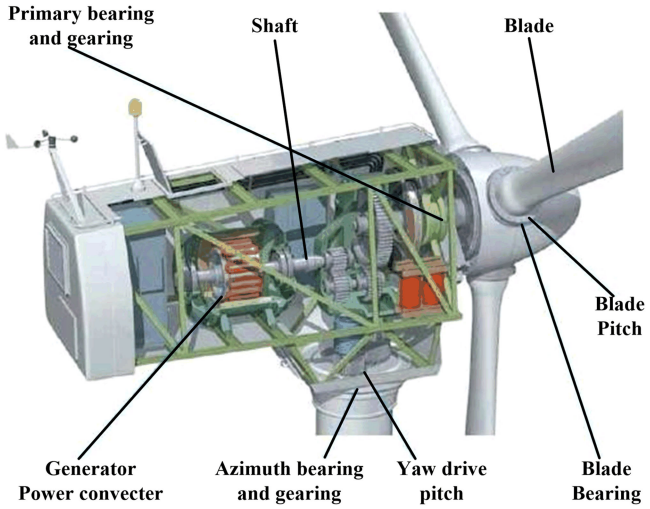

Fig. 1. Structure of a geared WT.

energy [1]–[4]. In order to improve the availability and reduce the operational and maintenance (O&M) cost [5], it is important to investigate condition monitoring (CM) [6], [7], fault diagnosis [8], nondestructive testing (NDT) [9], [10], and structural health monitoring [11] to support on-condition maintenance (OCM) for WTs [12]–[15].

As shown in Fig. 1, WTs are typical complex mechatronic systems [16]. Blade is considered to be one of the most critical components of the WTs, which encounters extremely complex loading sequences in-service. Once a blade has been built and installed, it is necessary to perform CM and frequent NDT to carry out OCM in order to find potential defects and avoid blade function failures [6], [12], [17]–[19]. Besnard and Bertling [20] investigated three maintenance strategies for WT blades. Many theoretical and practical OCM case studies have shown that online CM is the optimal maintenance strategy for components with high failure rates and short time to failure. In other cases, periodic or intermittent NDT and inspection is slightly more beneficial for low-failure-rate components [20]. In addition, periodic or intermittent NDT offers more feasible solutions than online CM for some complex structures due to technical limitations, cost and field restrictions. Carbon fiber reinforced plastics (CFRPs) are increasingly used to build WT blades [21]–[23]. Delaminations and disbonds are inevitable during either fabrication or in-service of a blade. It is difficult or even impossible to detect these inside damages using visual inspection (400–760 nm in wavelength) or machine vision (400–1100 nm in wavelength) based on CCD or CMOS [24]. Thus, new machine vision inspection and diagnosis techniques for these invisible types of damage are very important and attractive subjects in the WT field.

Infrared (IR) thermography (3–5 μm or 7–14 μm in wavelength) has become an important machine vision tool for nondestructive testing [9], [25]–[28] and fault diagnosis [29]. In recent years, it has also been explored for CM and for NDT of WT systems [30]–[32]. Manohar and Scalea [31] proposed lock-in thermography to detect wind turbine blades rapidly. In order to maximize the inspection area, Avdelidis *et al.* developed an autonomous and lightweight multi-axis scanning system [33]. Electromagnetic induction (EMI) and the Joule effect can be used for heating an electrically conducting object. With the help of EMI heating, induction infrared thermography (IIT) has been proposed specifically for conductive material inspection as it has many strengths including being nondestructive, noncontact, full field, fast speed, and high resolution [34], [35]. IIT has mainly two analysis methods: eddy current pulsed thermography (ECPT) [36] and eddy current pulsed phase thermography (ECPPT) [37]. Recently, ECPT's modeling was investigated for CFRP inspection [9], [38]–[40]. Also, ECPT's experimental studies were carried out for artificial crack [41] and impact [42] evaluation in CFRP [9], [43], [44]. With ECPPT, inner (subsurface) delaminations of areas 36 and 100 mm^2 could be effectively evaluated using phasegrams [45].

In photothermal imaging field, Mandelis and Tabatabaei proposed the thermal wave radar imaging (TWRI) to detect deep subsurface defects in metals and human dental caries demineralization lesions [46], [47]. The excitation signal of TWR is linear frequency modulated laser continuous wave and the signal processing is cross-correlation (CC) pulse compression and matched-filtering. The experimental results have shown that TWR has a significant improvement in depth resolution and dynamic range. Furthermore, Mandelis and Kaiplavil developed truncated-correlation photothermal coherence tomography (TC-PCT), which is based on similar signal processing with TWR, but with a time-evolving filter. TC-PCT enables three-dimensional (3-D) visualization [48], [49]. However, the TWR modality has not been used for CFRP inspections.

In this study, TWR based on a photothermal source and CC pulse compression and matched filtering as proposed by Mandelis *et al.* is introduced into IIT for imaging inspection and diagnosis of a CFRP blade. The paper after Introduction is organized as follows. First, the physical principle of IIT is introduced in Section II, and signal processing methods for ECPT, ECPPT, and the TWR modality are demonstrated in Section III. Then, the experimental system and specimen are introduced in Section IV, followed by comparative studies of delamination evaluations in Sections V and VI. Finally, comparisons among the various imaging methodologies, limitations, and conclusion are outlined in Section VII.

II. Principle of IIT

The physics-based principle of IIT mainly considers volumetric induction heating, conduction heat transfer and their interaction with various defects.

A. Volumetric Induction Heating

Fig. 2(a) shows the physical principle schematic of IIT for CFRP. The excitation signal of IIT is one period of high-frequency alternating current (AC) signal $I(t)$. The AC pulse signal is then driven into a coil along the material under testing (MUT, CFRP sample in this study). When passing through the coil, the AC pulse signal can induce eddy currents in the CFRP and then generate a resistive heat pulse $Q(t)$. These eddy currents are governed by electromagnetic induction within a penetration depth (aka skin depth, δ). It is estimated that δ for CFRP ($\sim$50 mm) is greater than the thickness of the CFRP sam-

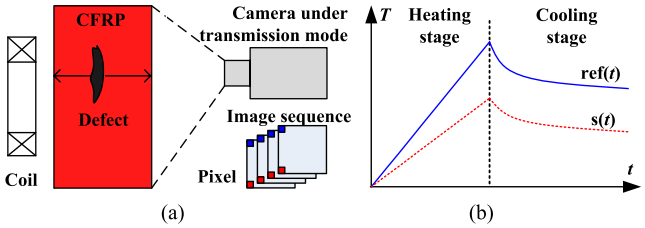

Fig. 2. (a) Physical principle schematic of IIT for CFRP. (b) Temperature response in ECPT.

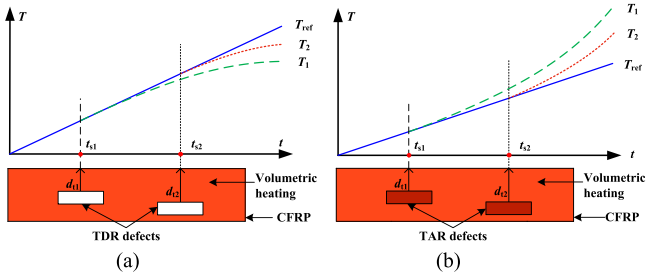

Fig. 3. VH and temperature responses for (a) TDR defects and (b) TAR defects. TDR defects: these defects do not generate heat or generate smaller amounts of heat than the base CFRP with the same volume. TAR defects: these defects generate more heat than the base CFRP with the same volume.

ple (<4 mm) in this study. Thus, the appropriate heating mode for CFRP is volumetric heating (VH). The generated resistive heat $Q(t)$ is governed by the following equation [41]:

$$Q = \frac{1}{\sigma}|J|^2 t = \frac{1}{\sigma}|\sigma E|^2 t \tag{1}$$

where J is the eddy current density, E the electric field intensity vector, and t is the heating time.

B. Heat Conduction

The resistive heat generation source $Q(t)$ will be simultaneously conducted in 3-D space as a time transient governed by [10]

$$\frac{\partial T}{\partial t} = \frac{k}{\rho C_p}\left(\frac{\partial^2 T}{\partial x^2} + \frac{\partial^2 T}{\partial y^2} + \frac{\partial^2 T}{\partial z^2}\right) + \frac{1}{\rho C_p} Q(t) \tag{2}$$

where ρ, C_p, and k are the density, heat capacity, and thermal conductivity, respectively. As heat conducts, the temperature T captured by IR camera on the surface of CFRP will changes to form a transient response. A transient temperature response is shown as the solid blue line [ref(t)] in Fig. 2(b). It can be divided into heating stage and cooling stage. The temperature due to VH increases approximately linearly during the heating stage, faster than surface heating. During the cooling stage, the VH temperature decreases approximately as an inverse power function and is slower than surface heating [50].

C. Interaction with Defects

According to (1) and (2), the defects inside CFRP, with different electric parameter (σ) and thermal parameters (C_p, k), will generate different heat $Q_{\rm d}(t)$ from the original heat source $Q_{\rm ref}(t)$ of the same volume base materials (CFRP) and thus affect the heat conduction process. Finally, the temperature response on the surface of CFRP will be different as shown with the dashed red line [$s(t)$] in Fig. 2(b). In this study, we consider defects as point heat sources, also with different electric parameters. According to the quantity of heat generation, we classify the defects into two kinds. One is defined as thermal depletion region (TDR) defects, another as thermal accumulation region (TAR) defects [51]. TDR defects do not generate heat (or they generate smaller amounts of heat than the base CFRP with the same volume) when CFRP is volumetrically heated. On the contrary, TAR defects generate more heat than the base CFRP with the same volume.

The abnormal thermal diffusion propagation caused by TDR and TAR defects determines the temperature response ($T(t)$) on the surface of a CFRP sample. We analyze the TDR defects first and then the TAR defects. As shown in Fig. 3(a), two TDR defects are located inside the CFRP sample at different depths d_{t1} and d_{t2} ($d_{t1} < d_{t2}$). These two defects' temperature responses (T_1 and T_2), shown as green and red dotted lines, diverge downward from $T_{\rm ref}$ (blue solid line) due to heat sinking from the surrounding material into the defects. Here, the times when T_1 and T_2 diverge from $T_{\rm ref}$ are defined as separation times t_{s1} and t_{s2}, respectively, as marked by red dots. According to heat conduction theory, the time-domain thermal diffusion length ($\mu \sim (\alpha t)^{1/2}$) is proportional to the square root of time $t^{1/2}$ (α is thermal diffusivity); therefore, we can qualitatively conclude that t_{s1} is smaller than t_{s2}, because d_{t1} is shorter than d_{t2}. As shown in Fig. 3(b), in the opposite case, two TAR defects are located in CFRP at depths d_{t1} and d_{t2} ($d_{t1} < d_{t2}$). Temperature responses above these two defects (T_1 and T_2), shown as green and red dotted lines, will diverge upward from $T_{\rm ref}$ (blue solid line), which is the opposite behavior of Fig. 3(a). However, similarly to Fig. 3(a), t_{s1} is smaller than t_{s2} because d_{t1} is shorter than d_{t2}. It can be concluded that separation time has a monotonic relationship with defect depth, as expected, and can be used to measure the depth of subsurface objects of interest in MUT. Another advantage of VH is that defect-altered heat conduction directly from defect to surface does not accumulate or deplete at the interface like surface heating thermography. As a result, the presence of the defect appears earlier than in surface heating thermography.

III. Signal Processing

The signal processing methods for ECPT, ECPPT, and TWR are totally different as demonstrated in this section.

A. ECPT and ECPPT

With ECPT, the differential temperature response is defined as

$$\Delta s(t) = s(t) - {\rm ref}(t) \tag{3}$$

where $s(t)$ is the temperature response of a pixel and ref(t) is the reference temperature response of a nondefective pixel. The thermogram formed by all pixels of $s(t)$ or $\Delta s(t)$ at some time can be used to detect the damages in CFRP.

ECPPT's signal processing is based on the Fourier transform of ECPT. After obtaining phase spectra $\varphi(\omega)$ for all pixels using

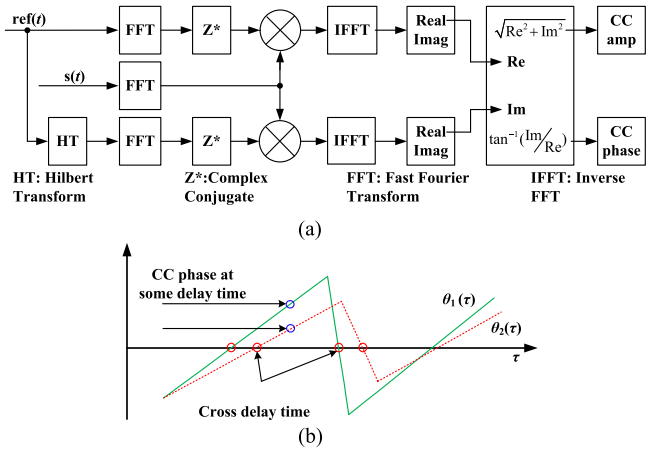

Fig. 4. (a) TWR imaging signal processing block diagram. (b) TWR phase delay traces.

a discrete Fourier transform (DFT), the differential phase spectra can be obtained from

$$\Delta\varphi(\omega) = \varphi(\omega) - \varphi_{\text{ref}}(\omega) \tag{4}$$

where $\varphi(\omega)$ is the phase spectrum for one detected signal $s(t)$. $\varphi_{\text{ref}}(\omega)$ is the phase spectrum of the reference signal ref(t). Phase images (phasegrams) constructed from the single-ended or the differential phases at some frequencies are used for imaging inspection of the MUT.

B. Thermal-Wave Radar Imaging Modality

Fig. 4(a) shows the schematic for TWR modality [46], [47], [52], [53]. The equation to calculate the TWR amplitude (CC) of two signals ref(t) and $s(t)$ is shown as follows:

$$\text{CC}(\tau) = F^{-1}\{REF(\omega)^* S(\omega)\} \tag{5}$$

where REF(ω) is the Fourier transforms of ref(t) and $S(\omega)$ is the Fourier transforms of $s(t)$. The symbol $*$ denotes the complex conjugation. F^{-1} denote the inverse Fourier transform operators, and τ is the time delay between ref(t) and $s(t)$. The differential TWR CC (ΔCC) can be calculated easily using the following equation:

$$\Delta\text{CC}(\tau) = \text{CC}(\tau) - \text{CC}_{\text{ref}}(\tau). \tag{6}$$

The TWR amplitude (CC) strongly depends on the temperature and emissivity. TWR phase (θ) can be calculated from (7)

$$\theta(\tau) = \frac{F^{-1}\{\text{REF}(\omega)^* S(\omega)\}}{F^{-1}\{[-i\text{sgn}(\omega)\text{REF}(\omega)]^* S(\omega)\}} \tag{7}$$

where sgn(ω) is the signum function and i is the imaginary unit. The significance of the TWR phase (θ) is that it is an emissivity-independent and time-delay-dependent quantity [46]. The differential TWR phase ($\Delta\theta$) can be calculated according to (8)

$$\Delta\theta(\tau) = \theta(\tau) - \theta_{\text{ref}}(\tau) \tag{8}$$

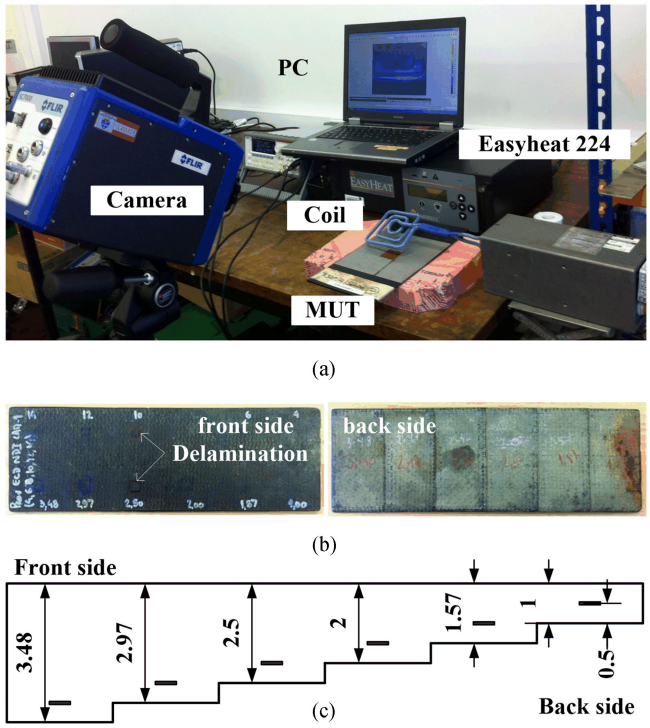

Fig. 5. (a) IIT setup. (b) Front and back side of CFRP specimen. (c) Section schematic of CFRP specimen.

where $\theta_{\text{ref}}(\tau)$ is the reference TWR phase. Correspondingly, $\Delta\theta(\tau)$ is a emissivity-independent and time-delay dependent quantity.

Two TWR phase delay traces $\theta_1(\tau)$ and $\theta_2(\tau)$ are shown in Fig. 4(b). Clearly, the value of TWR phases at some delay times are different, as marked by the blue circle. The feature named cross-delay time (CDT) can also be extracted and defined as the time when the TWR phase crosses the horizontal ordinate during the increasing and decreasing stages, as marked by red circle.

In the next section, the temperature data captured by the IR camera and processed on a PC using ECPT, ECPPT, and TWR, respectively, will be described.

IV. Experimental Setup

The experimental system for IIT was developed, as shown in Fig. 5(a), which consists of a precision induction heating device, a coil, and an IR camera. The excitation coil was designed as a rectangular planar shape and one side was close to CFRP with a distance ~1 mm for heating (this side is defined as the heating side). In experiments, we used digital level (DL) of radiation as the unit of temperature [37]. Photographs and a cross-sectional schematic of CFRP sample are shown in Fig. 5(b) and (c), respectively. The lateral dimensions of CFRP specimen were 300 × 100 mm^2. The CFRP specimen had six areas with varying thicknesses from 3.48, 2.97, 2.5, 2.0, 1.57, to 1 mm. Two polytetrafluoroethylene films (36 and 100 mm^2 in lateral size) were inserted in each thickness area to simulate delaminations. The longitudinal distance between these two delamination

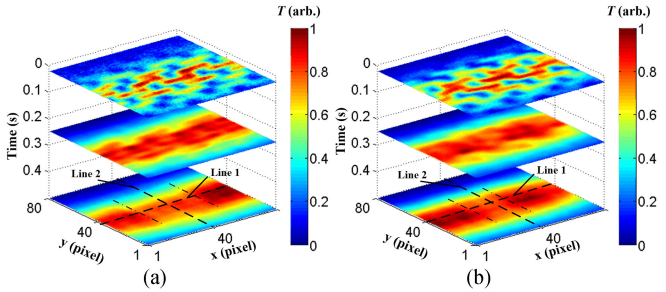

Fig. 6. (a) Thermograms for 100 mm^2 delamination. (b) Thermograms for 36 mm^2 delamination. The unit of temperature is DL and is normalized to [0, 1].

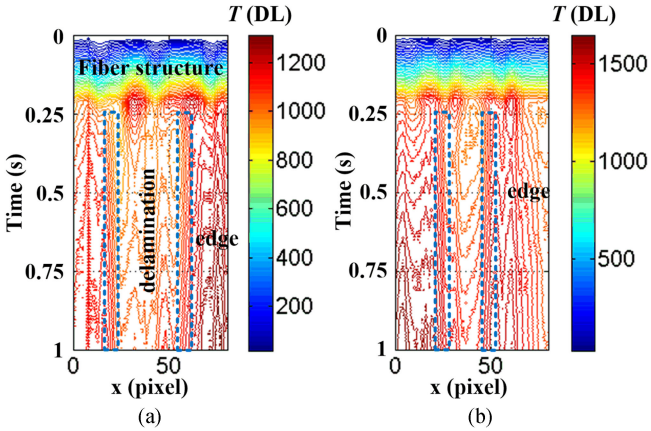

Fig. 7. B-scan image of line 1 over (a) 100 mm^2 and (b) 36 mm^2 delaminations. The unit of temperature is DL.

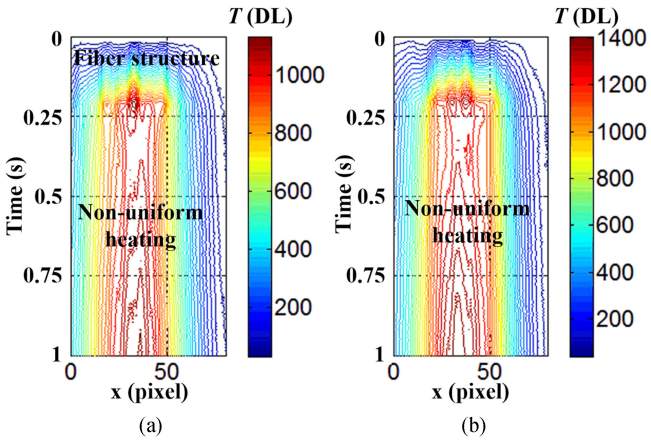

Fig. 8. B-scan image of line 2 over (a) 100 mm^2 and (b) 36 mm^2 delaminations. The unit of temperature is DL.

defects in each area was ∼70 mm. These delaminations had the same distance (0.5 mm) to the back side of CFRP but different distances (2.98, 2.47, 2.0, 1.5, 1.07, and 0.5 mm) to the front side.

V. Experimental Results and Discussion

In experiments, the heating side of coil was placed close to the front side of the CFRP specimen with a distance ∼1 mm while the IR camera was placed on the back side with a distance ∼0.5 m. The heating time and the cooling time were set to be 0.2 and 0.8 s, respectively. Two delaminations in the thickest area (3.48 mm) were tested using ECPT and TWR.

A. ECPT Imaging and Tomography in Time Domain

Using the established ECPT modality, thermograms at different instants can be obtained as a form of time tomography (slicing). Fig. 6(a) shows several thermograms for a 100 mm^2 delamination at 25 ms, 0.25 s, and 0.5 s, respectively. Fig. 6(b) shows several thermograms for a 36 mm^2 delamination at 25 ms, 0.25 s, and 0.5 s, respectively. Clearly, there is a distinct NHE along the y-direction, which is perpendicular to the heating side of the excitation coil. Carbon fiber-woven structures can be observed through hot and cold (dark) patterns from the thermogram at 0.025 s. In detail, the carbon fibers are at high temperature and thus highlighted in red color because they are directly heated by the inductive eddy currents. In the thermogram at 0.25 s, the highlighted area caused by the FWS is blurred but is still visible. In the thermogram at 0.5 s, a relatively low temperature area caused by delamination appears and the delamination width in the x-direction can be evaluated as shown between two dotted-dashed lines. However, it is impossible to evaluate the delamination's plane shape, especially in the y-direction due to severe NHE.

Two straight lines were drawn over the delamination areas in Fig. 6. Line 1 is parallel to the heating side of the excitation coil, while line 2 is vertical to the heating side of the inductive coil. Every pixel point on the two lines has a transient temperature response, like $s(t)$ and ref(t). This is an A-scan as shown in Fig. 2(b). One coordinate means time, and the other coordinate means the temperature. A collection of A-scans of all points in one line displayed in a graph yields a B-scan image, which can show sectional information of an MUT. In a B-scan graph, one coordinate denotes the position of a point and the other coordinate denotes the A-scan time. The amplitude of the A-scan is indicated by an associated color. According to the color distribution or contour line shape, any abnormal temperature due to the presence of defects can be identified from the B-scan. Fig. 7 shows B-scan images of line 1 over the 100 and 36 mm^2 delaminations. Because line 1 is parallel to the heating side of the coil, there is little NHE along line 1. The contour lines before 0.1 s just show the periodic FWS. The delamination edge in the x-direction could be identified from the contour lines after 25 ms by the abnormal contour shapes, as marked by dashed lines. Therefore, the width of two delaminations (sizes in the x-direction were 10 and 6 mm) can be measured from the number of pixels between the two dashed lines. Fig. 8 shows B-scan images of line 2 over the 100 and 36 mm^2 delaminations of Fig. 6. Similar to line 1, the contour lines of line 2 before 0.1 s show the periodic FWS. However, line 2 is vertical to the heating side of the coil, therefore NHE dominates so that the temperature gradient of line 2 is huge and temperature variations caused by delaminations are concealed. As a result, it is impossible to

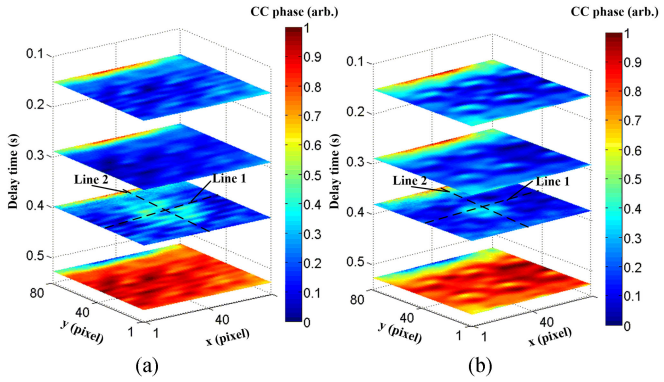

Fig. 9. TWR phase images of (a) the 100 mm^2 delamination and (b) the 36 mm^2 delamination at 0.1523, 0.2895, 0.3991 and 0.5271 s. The unit of TWR phase is rad and is normalized to [0, 1].

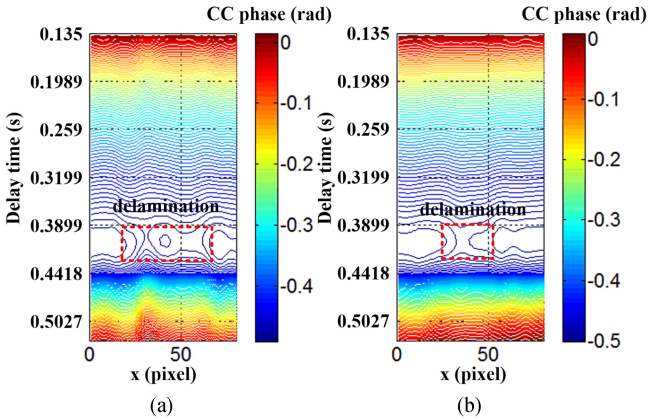

Fig. 10. B-scan images from the TWR phase of line 1 over (a) 100 mm^2 and (b) 36 mm^2 delaminations. The unit of TWR phase is rad.

evaluate the delamination's size in y-direction due to the severe NHE.

B. TWR Imaging and Tomography

Temperature responses during the cooling stage for two delaminations were processed by the TWR imaging modality as discussed in Section III. The two-dimensional (2-D) TWR phase images at different delay times could be obtained as a form of delay time tomography. Fig. 9(a) shows several TWR phase images of 100 mm^2 delamination at 0.1523, 0.2895, 0.3991, and 0.5271 s. Fig. 9(b) shows several TWR phase images of 36 mm^2 delamination at 0.1523, 0.2895, 0.3809, and 0.5271 s. The unit of TWR phase is rad and is normalized to the range [0, 1]. It can be observed that not only NHE but also FWS can be eliminated from the TWR phase images. Furthermore, the shapes of the two delaminations can be identified through the TWR phase images at 0.3991 and 0.3809 s, respectively. In summary, it is concluded that delamination detectability can be much improved with TWR imaging compared with the ECPT results in Fig. 6.

The B-scan images of the same line 1 of the 100 and 36 mm^2 delaminations are shown in Fig. 10, and those for the same line 2 of the 100 and 36 mm^2 delaminations are shown in Fig. 11. Clearly, the contour lines in Figs. 10 and 11 are smoother than those in Figs. 7 and 8. This implies that both NHE and FWS could be suppressed, and thus, the delamination's size in both x- and y-directions can be evaluated easily as marked by the dashed rectangles.

The TWR phase delay traces $\theta(\tau)$ at four points were also captured, as shown in Fig. 12(a). Table I shows their locations. As mentioned earlier, the FWS is visible in the thermogram at 0.025 s and the low-temperature area caused by delamination appears in the thermogram at 0.5 s. First, we enlarged the thermogram at 0.5 s and confirmed that points A and B are on defect-free areas and points C and D are on the 100 mm^2 delamination area. Next, we enlarged the thermogram at 0.025 s and confirmed that points A and C are on the matrix area and points B and D on the carbon fiber bundle. Because point A is on the defect-free area and the matrix, we took point A as the reference

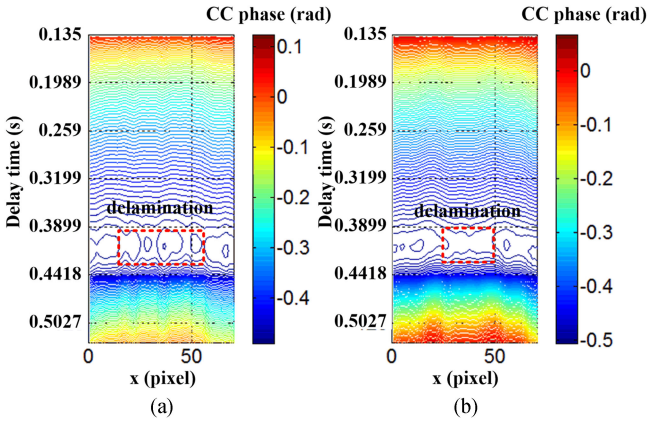

Fig. 11. B-scan images of the TWR phase of line 2 over (a) 100 mm^2 and (b) 36 mm^2 delaminations. The unit of TWR phase is rad.

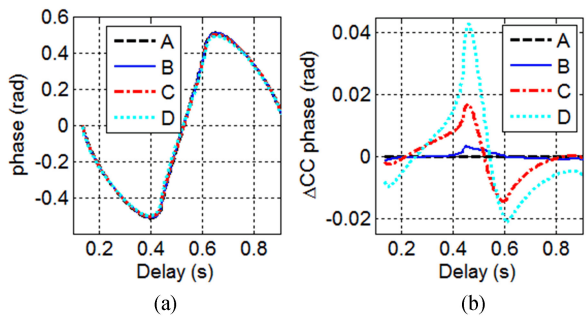

Fig. 12. (a) TWR phase traces and (b) differential TWR phase traces for four points. The unit of TWR phase is rad.

TABLE I
LOCATION OF POINTS A, B, C, AND D

Point name	Location (Carbon fiber bundle or matrix)	Location (Delamination or good part)
A	Matrix	Defect-free
B	Carbon fiber bundle	Defect-free
C	Matrix	Delamination
D	Carbon fiber bundle	Delamination

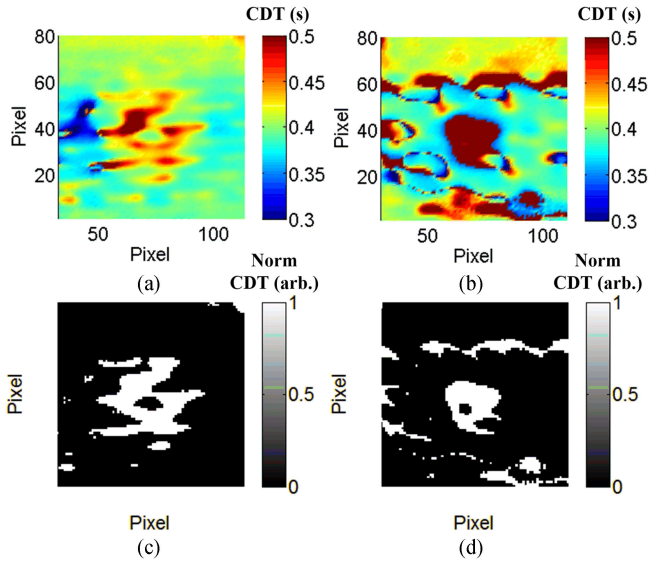

Fig. 13. Images formed from TWR CDT for (a) 100 and (b) 36 mm^2 delaminations. The binarized images formed from CDT for (c) 100 mm^2 and (d) 36 mm^2 delaminations.

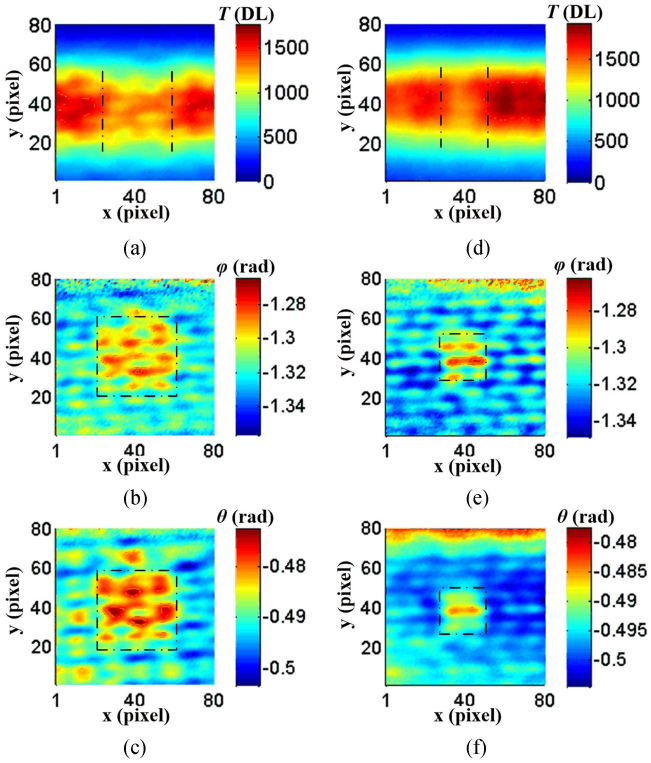

Fig. 14. Imaging results for two delaminations in 2.97 mm thickness. (a) ECPT thermogram at 0.5 s, (b) ECPPT phasegram at 3.125 Hz, and (c) TWR phasegram at 0.4083 s for 100 mm^2 delamination. (d) ECPT thermogram at 0.5 s, (e) ECPPT phasegram at 3.125 Hz, and (f) TWR phasegram at 0.3687 s for the 36 mm^2 delamination.

TWR phase $\theta_{\text{ref}}(\tau)$ in (8). Point B on the defect-free area and the carbon fiber bundle could also be selected as an alternative reference TWR phase. The effects of different reference signals on TWR imaging will be investigated in the future. The differential TWR phase delay traces $\Delta\theta(\tau)$ for these points are shown in Fig. 12(b). Clearly, the TWR phases at delay times from 0.3 to 0.8 s are different. The feature named CDT can be extracted from the differential TWR phase traces when they cross the horizontal ordinate during the decreasing stage. Clearly, the values of CDT for points B, C, and D are different. Thus, the CDT feature can be used for highly resolved delamination imaging.

The images and binarized images for two delaminations formed from the TWR CDT are shown in Fig. 13. The shapes of the two delaminations can be clearly identified. After binarization, the sizes (or areas) of the two delaminations could also be measured using a conventional algorithm in machine vision.

In summary, it can be concluded from the ECPT and TWR imaging results for a delamination in the 3.48 mm-thick area that NHE and FWS can all be suppressed through TWR phase imaging. As a result, the delaminations plane shape identification performance can be improved considerably over ECPT.

VI. Other Image Comparison Studies

Keeping the same experimental conditions, delaminations in the 2.97-, 1.57-, and 1-mm-thick area were tested for comparison studies. Besides ECPT and TWR, the ECPPT modality proposed in [45] was also used for comparison. Fig. 14 shows the ECPT thermograms and ECPPT and TWR phasegrams for delaminations in a 2.97-mm-thick area. In the ECPT thermograms in Fig. 14(a) and (d), the delaminations' widths along the coil can be evaluated while the delaminations' shape can be identified through the ECPPT phasegrams in Fig. 14(b) and (e), and the TWR phasegrams in Fig. 14(c) and (f). As shown in Table II, it is obvious that the TWR results have the highest signal-to-noise ratio (SNR means the ratio between delamination and surrounding area in this study), best shape identification, and best elimination of NHE in the three modalities (ECPT, ECPPT, and TWR) for delamination identification. In addition, ECPPT has the best detail observation performance.

TABLE II
Qualitative Comparison Between ECPT, ECPPT, and TWR

	Thickness	ECPT	ECPPT	TWR
SNR	2.97 mm	no	better	best
Shape identification		no	better	best
Elimination of NHT		no	better	best
Detail observation		no	best	better
SNR	1.57 mm	no	better	best
Shape identification		no	better	best
Elimination of NHT		no	better	best
Detail observation		no	best	better
SNR	1 mm	no	best	better
Shape identification		no	better	best
Elimination of NHT		no	better	best
Detail observation		no	best	better

Fig. 15 shows the ECPT thermogram, ECPPT phasegram, and TWR phasegram for two delaminations in a 1.57-mm-thick area. Obviously, the delamination's shape can be identified through the ECPPT phasegram in Fig. 15(b) and (e), and the TWR phasegram in Fig. 15(c) and (f). It is clear that the TWR results are better than ECPPT. As shown in Table II, imaging contrast (the ratio between delamination and surrounding area), shape

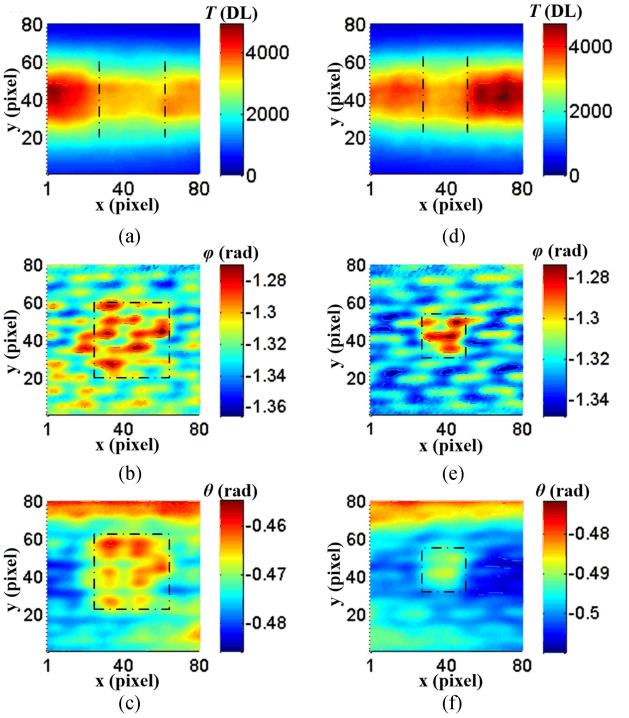

Fig. 15. Results for delaminations in the 1.57 mm thickness area. (a) ECPT thermogram at 0.5 s, (b) ECPPT phasegram at 3.125 Hz, and (c) TWR phasegram at 0.3717 s for the 100 mm^2 delamination. (d) ECPT thermogram at 0.5 s, (e) ECPPT phasegram at 3.125 Hz, and (f) TWR phasegram at 0.3626 s for the 36 mm^2 delamination.

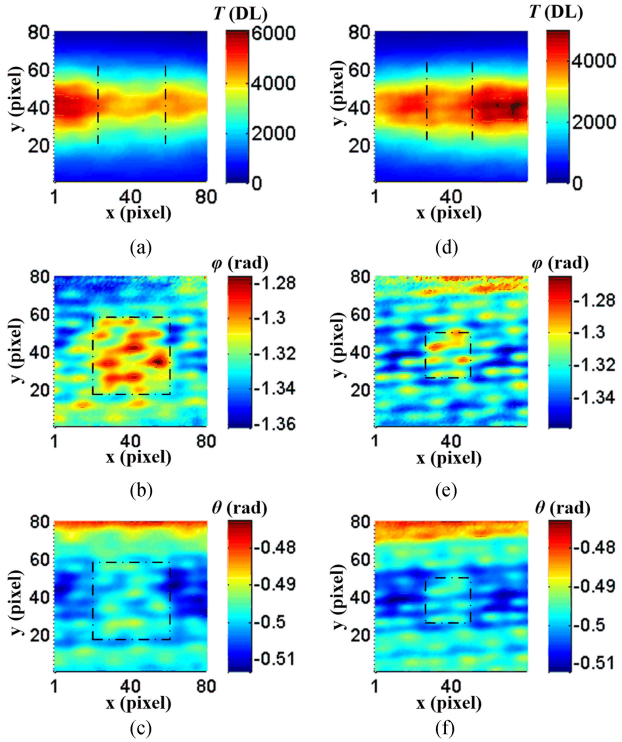

Fig. 16. Results for delaminations in 1 mm thickness area. (a) ECPT thermogram at 0.5 s, (b) ECPPT phasegram at 3.125 Hz, and (c) TWR phasegram at 0.3961 s for the 100 mm^2 delamination. (d) ECPT thermogram at 0.5 s, (e) ECPPT phasegram at 3.125 Hz, and (f) TWR phasegram at 0.3930 s for the 36 mm^2 delamination.

identification, and elimination of NHE of TWR for delaminations in the 1.57-mm-thick area are better than those of ECPPT. However, ECPPT exhibits the best detail observation performance. Fig. 16 shows the ECPT thermogram, ECPPT phasegram, and TWR phasegram for a delamination in the 1-mm-thick area. Delamination shape could be identified through the ECPPT phasegram in Fig. 16(b) and (e) and the TWR phasegram in Fig. 16(c) and (f). As shown in Table II, the shape identification and elimination of NHE of TWR for delaminations in the 1-mm-thick area are better than those of ECPPT. However, ECPPT also shows the best detail observation performance and contrast. It is found that the TWR contrast for 1 mm thickness (smallest) is not optimal among the three thickness images. Logically, signal attenuation should be stronger in thicker structures. The reason behind this phenomenon is the VH distribution of CFRP. It is too shallow in the 1-mm-thick area so that the heating quantity and contrast are lowest. Thus, temperature contrast caused by the carbon fiber structures dominates. The effects of thickness on detection performance remain a topic for future investigations.

It can be concluded from the earlier results that NHE and FWS can all be suppressed through the TWR imaging modality, thereby leading to enhanced improvements for delamination shape identification and SNR contrast over ECPT and ECPPT. However, under the VH conditions of our samples, the TWR mode performs worse than ECPPT in eliminating NHE faraway from the coil. It is clear that the shorter the heat conduction path, the weaker the contrast produced making the detection of the delaminated area more challenging. Thermal-wave confinement within thinner structures tends to enhance TWR signals generated on material surfaces with photothermal heating sources like lamps; however, the eddy current heating modality produces a subsurface source which may require frequency bandwidth and eddy current intensity adjustments so that the TWR thermal diffusion length (defined as the frequency chirp repetition rate) will lie within the eddy current excited thickness at an acceptable SNR.

VII. Conclusion and Future Work

In this study, TWR signal generation and processing was introduced to IIT-based machine vision and was used for blade CFRP imaging inspection. This modality was implemented experimentally in the transmission mode and compared with existing ECPT and ECPPT. Two conclusions were reached:

1) Both phasegrams using ECPPT and TWR methods could reduce NHE caused by coil shape and periodic carbon fiber structures. The imaging SNR contrast and shape detection performance of the TWR was higher than ECPT and ECPPT.
2) 36 mm^2 delaminations in CFRP with thickness varying from 1.0 to 3.5 mm could be effectively detected and shapes recovered using IIT and TWR in the transmission mode. Because the inspection methods under transmission and reflection modes are similar for CFRP due to VH [45], it is concluded that these delaminations can be inspected in reflection mode.

However, there are some limitations in the current experimental set-up. One is that the depths of defects could not be quantitatively evaluated using the TWR. This is a limitation of the current experimental system which cannot transmit chirps of variable frequency bandwidths or produce TWR signals with acceptable SNR. Therefore, the potential advantages of three-dimensional reconstruction of subsurface features as enabled by TC-PCT [46], [48], [54], [55] could not be implemented and exploited. In addition, the detectable depths for ECPPT and TWR remain shallow (several millimeters) due to the physics of the heavily spatially damped thermal-wave diffusion. For spar cap detection in wind blades, ultrasonic testing (including laser ultrasound) or X-rays would be better choices than thermography. Future work will include the following: 1) the optimization of thermal-wave-radar excitation signals ("waveform engineering") in experimental systems to transmit chirps with variable widths which can produce improved axial resolution and adjustable frequency bandwidths; 2) an adaptation of the TC-PCT algorithm to CFRP inspection to enhance depth penetration and develop 3-D thermophotonic imaging; 3) depth quantitation (object distance ranging) verification; 4) scanning IIT for online quality control; and 5) *in situ* automated thermography inspection with robotics.

Acknowledgment

The authors would like to thank Prof. G. Y. Tian with Newcastle University, U.K., for help in experimental studies.

References

[1] H. Sanchez, T. Escobet, V. Puig, and P. F. Odgaard, "Fault Diagnosis of an advanced wind turbine benchmark using interval-based ARRs and observers," *IEEE Trans. Ind. Electron.*, vol. 62, no. 6, pp. 3783–3793, Jun. 2015.

[2] L. Wang, Z. Zhang, H. Long, J. Xu, and R. Liu, "Wind turbine gearbox failure identification with deep neural networks," *IEEE Trans. Ind. Informat.*, vol. 13, no. 3, pp. 1360–1368, Jun. 2017.

[3] X. Liu, Z. Gao, and M. Z. Q. Chen, "Takagi–Sugeno Fuzzy model based fault estimation and signal compensation with application to wind turbines," *IEEE Trans. Ind. Electron.*, vol. 64, no. 7, pp. 5678–5689, Jul. 2017.

[4] W. Yang, P. J. Tavner, C. J. Crabtree, and M. Wilkinson, "Cost-effective condition monitoring for wind turbines," *IEEE Trans. Ind. Electron.*, vol. 57, no. 1, pp. 263–271, Jan. 2010.

[5] S. Simani, S. Farsoni, and P. Castaldi, "Fault diagnosis of a wind turbine benchmark via identified fuzzy models," *IEEE Trans. Ind. Electron.*, vol. 62, no. 6, pp. 3775–3782, Jun. 2015.

[6] W. Yang, Z. Lang, and W. Tian, "Condition monitoring and damage location of wind turbine blades by frequency response transmissibility analysis," *IEEE Trans. Ind. Electron.*, vol. 62, no. 10, pp. 6558–6564, Oct. 2015.

[7] W. Yang, P. J. Tavner, and W. Tian, "Wind turbine condition monitoring based on an improved spline-kernelled Chirplet transform," *IEEE Trans. Ind. Electron.*, vol. 62, no. 10, pp. 6565–6574, Oct. 2015.

[8] W. Qiao and D. Lu, "A survey on wind turbine condition monitoring and fault diagnosis—Part I: Components and subsystems," *IEEE Trans. Ind. Electron.*, vol. 62, no. 10, pp. 6536–6545, Oct. 2015.

[9] L. Cheng and G. Y. Tian, "Transient thermal behavior of eddy-current pulsed thermography for nondestructive evaluation of composites," *IEEE Trans. Instrum. Meas.*, vol. 62, no. 5, pp. 1215–1222, May 2013.

[10] B. Gao, Y. He, W. L. Woo, G. Y. Tian, J. Liu, and Y. Hu, "Multidimensional tensor-based inductive thermography with multiple physical fields for offshore wind turbine gear inspection," *IEEE Trans. Ind. Electron.*, vol. 63, no. 10, pp. 6305–6315, Oct. 2016.

[11] M. Moradi and S. Sivoththaman, "MEMS multisensor intelligent damage detection for wind turbines," *IEEE Sensors J.*, vol. 15, no. 3, pp. 1437–1444, Mar. 2015.

[12] L. Wang and Z. Zhang, "Automatic detection of wind turbine blade surface cracks based on UAV-taken images," *IEEE Trans. Ind. Electron.*, vol. 64, no. 9, pp. 7293–7303, Sep. 2017.

[13] S. Huang, X. Wu, X. Liu, J. Gao, and Y. He, "Overview of condition monitoring and operation control of electric power conversion systems in direct-drive wind turbines under faults," *Frontiers of Mech. Eng.*, vol. 12, pp. 281–302, 2017.

[14] Z. Shuai, C. Shen, X. Yin, X. Liu, and Z. J. Shen, "Fault analysis of inverter-interfaced distributed generators with different control schemes," *IEEE Trans. Power Del.*, vol. 33, no. 3, pp. 1223–1235, Jun. 2018.

[15] Z. Shuai, W. Huang, C. Shen, J. Ge, and Z. J. Shen, "Characteristics and restraining method of fast transient inrush fault currents in synchronverters," *IEEE Trans. Ind. Electron.*, vol. 64, no. 9, pp. 7487–7497, Sep. 2017.

[16] S. Yin, X. Li, H. Gao, and O. Kaynak, "Data-based techniques focused on modern industry: An overview," *IEEE Trans. Ind. Electron.*, vol. 62, no. 1, pp. 657–667, Jan. 2014.

[17] R. Yang, Y. He, and H. Zhang, "Progress and trends in nondestructive testing for wind turbine composite blade," *Renew. Sustain. Energy Rev.*, vol. 60, pp. 1225–1250, 2016.

[18] S. Zhang, O. Franek, P. C. F. Eggers, C. Byskov, and G. F. Pedersen, "Multipath suppression with an absorber for UWB wind turbine blade deflection sensing systems," *IEEE Trans. Microw. Theory Tech.*, vol. 65, no. 7, pp. 1–13, Jul. 2017.

[19] G. L. Dong, S. Oh, and H. I. Son, "Maintenance robot for 5-MW offshore wind turbines and its control," *IEEE/ASME Trans. Mechatronics*, vol. 21, no. 5, pp. 2272–2283, Oct. 2016.

[20] F. Besnard and L. Bertling, "An approach for condition-based maintenance optimization applied to wind turbine blades," *IEEE Trans. Sustain. Energy*, vol. 1, no. 2, pp. 77–83, Jul. 2010.

[21] F. Rachidi *et al.*, "A review of current issues in lightning protection of new-generation wind-turbine blades," *IEEE Trans. Ind. Electron.*, vol. 55, no. 6, pp. 2489–2496, Jun. 2008.

[22] W. L. Li, H. B. Qiu, X. C. Zhang, J. C. Cao, and R. Yi, "Analyses on electromagnetic and temperature fields of superhigh-speed permanent-magnet generator with different sleeve materials," *IEEE Trans. Ind. Electron.*, vol. 61, no. 6, pp. 3056–3063, Jun. 2014.

[23] C. Tang, G. Y. Tian, K. Li, R. Sutthaweekul, and J. Wu, "Smart compressed sensing for online evaluation of CFRP structure integrity," *IEEE Trans. Ind. Electron.*, vol. 64, no. 12, pp. 9608–9617, Dec. 2017.

[24] M. Dema, C. Turner, H. Sari-Sarraf, and E. Hequet, "Machine vision system for characterizing horizontal wicking and drying using an infrared camera," *IEEE Trans. Ind. Informat.*, vol. 12, no. 2, pp. 493–502, Apr. 2016.

[25] H. Zhang *et al.*, "Optical and mechanical excitation thermography for impact response in basalt-carbon hybrid fiber-reinforced composite laminates," *IEEE Trans. Ind. Informat.*, vol. 14, pp. 514–522, Feb. 2018.

[26] H. Zhang *et al.*, "An experimental and analytical study of micro-laser line thermography on micro-sized flaws in stitched carbon fiber reinforced polymer composites," *Composites Sci. Technol.*, vol. 126, pp. 17–26, 2016.

[27] Y. He, R. Yang, X. Wu, and S. Huang, "Dynamic scanning electromagnetic infrared thermographic analysis based on blind source separation for industrial metallic damage evaluation," *IEEE Trans. Ind. Informat.*, to be published, doi: 10.1109/TII.2018.2822293.

[28] Y. He, B. Du, and S. Huang, "Non-contact electromagnetic induction excited infrared thermography for photovoltaic cells and modules inspection," *IEEE Trans. Ind. Informat.*, to be published, doi: 10.1109/TII.2018.2822272.

[29] E. Karakose, M. T. Gencoglu, M. Karakose, I. Aydin, and E. Akin, "A new experimental approach using image processing based tracking for an efficient fault diagnosis in pantograph-catenary systems," *IEEE Trans. Ind. Informat.*, vol. 13, no. 2, pp. 635–643, 2016.

[30] S. Stipetic, M. Kovacic, Z. Hanic, and M. Vrazic, "Measurement of excitation winding temperature on synchronous generator in rotation using infrared thermography," *IEEE Trans. Ind. Electron.*, vol. 59, no. 5, pp. 2288–2298, May 2012.

[31] A. Manohar and F. L. di Scalea, "Detection of defects in wind turbine composite blades using statistically enhanced Lock-In Thermography," *Struct. Health Monitoring*, vol. 12, pp. 566–574, Sep. 2013.

[32] Y. He, S. Chen, D. Zhou, S. Huang, and P. Wang, "Shared excitation based nonlinear ultrasound and vibro-thermography testing for CFRP barely visible impact damage inspection," *IEEE Trans. Ind. Informat.*, to be published, doi: 10.1109/TII.2018.2820816.

[33] N. P. Avdelidis, C. Ibarra-Castanedo, and X. P. V. Maldague, "Infrared thermography inspection of glass reinforced plastic (GRP) wind turbine blades and the concept of an automated scanning device," *presented at the Thermosense: Thermal Infrared Applications XXXV*, Baltimore, MD, USA, 2013.
[34] B. Gao, L. Bai, W. L. Woo, G. Y. Tian, and Y. Cheng, "Automatic defect identification of Eddy current pulsed thermography using single channel blind source separation," *IEEE Trans. Instrum. Meas.*, vol. 63, no. 4, pp. 913–922, Apr. 2014.
[35] B. Gao, W. L. Woo, Y. He, and G. Y. Tian, "Unsupervised sparse pattern diagnostic of defects with inductive thermography imaging system," *IEEE Trans. Ind. Informat.*, vol. 12, no. 1, pp. 371–383, Feb. 2016.
[36] K. Li, G. Y. Tian, L. Cheng, A. Yin, W. Cao, and S. Crichton, "State detection of bond wires in IGBT modules using eddy current pulsed thermography," *IEEE Trans. Power Electron.*, vol. 29, no. 9, pp. 5000–5009, Sep. 2014.
[37] Y. He, G. Y. Tian, M. Pan, and D. Chen, "Eddy current pulsed phase thermography and feature extraction," *Appl. Phys. Lett.*, vol. 103, p. 084104, 2013.
[38] B. Ramdane, D. Trichet, M. Belkadi, T. Saidi, and J. Fouladgar, "Electromagnetic and thermal modeling of composite materials using multilayer shell elements," *IEEE Trans. Magn.*, vol. 47, pp. 1134–1137, 2011.
[39] G. Wasselynck, D. Trichet, B. Ramdane, and J. Fouladgar, "Microscopic and macroscopic electromagnetic and thermal modeling of carbon fiber reinforced polymer composites," *IEEE Trans. Magn.*, vol. 47, no. 5, pp. 1114–1117, May 2011.
[40] B. H. Kien, G. Wasselynck, D. Trichet, B. Ramdane, G. Berthiau, and J. Fouladgar, "3-D modeling of thermo inductive non destructive testing method applied to multilayer composite," *IEEE Trans. Magn.*, vol. 49, no. 5, pp. 1949–1952, May 2013.
[41] L. Cheng and G. Y. Tian, "Surface crack detection for carbon fiber reinforced plastic (CFRP) materials using pulsed eddy current thermography," *IEEE Sensors J.*, vol. 11, no. 12, pp. 3261–3268, Dec. 2011.
[42] M. Pan, Y. He, G. Y. Tian, D. Chen, and F. Luo, "Defect characterisation using pulsed eddy current thermography under transmission mode and NDT applications," *NDT & E Int.*, vol. 52, pp. 28–36, 2012.
[43] Y. He, G. Tian, M. Pan, and D. Chen, "Impact evaluation in carbon fiber reinforced plastic (CFRP) laminates using eddy current pulsed thermography," *Composite Struct.*, vol. 109, pp. 1–7, 2014.
[44] W. Ren, J. Liu, G. Y. Tian, B. Gao, L. Cheng, and H. Yang, "Quantitative non-destructive evaluation method for impact damage using eddy current pulsed thermography," *Composites Part B: Eng.*, vol. 54, pp. 169–179, 2013.
[45] Y. He and R. Yang, "Eddy current volume heating thermography and phase analysis for imaging characterization of interface delamination in CFRP," *IEEE Trans. Ind. Informat.*, vol. 11, no. 6, pp. 1287–1297, Dec. 2015.
[46] N. Tabatabaei, A. Mandelis, and B. T. Amaechi, "Thermophotonic radar imaging: An emissivity-normalized modality with advantages over phase lock-in thermography," *Appl. Phys. Lett.*, vol. 98, p. 163706, 2011.
[47] N. Tabatabaei and A. Mandelis, "Thermal-wave radar: A novel subsurface imaging modality with extended depth-resolution dynamic range," *Rev. Sci. Instrum.*, vol. 80, p. 034902, 2009.
[48] S. Kaiplavil and A. Mandelis, "Truncated-correlation photothermal coherence tomography for deep subsurface analysis," *Nat. Photon.*, vol. 8, pp. 635–642, 2014.
[49] P. Tavakolian, K. Sivagurunathan, and A. Mandelis, "Enhanced truncated-correlation photothermal coherence tomography with application to deep subsurface defect imaging and 3-dimensional reconstructions," *J. Appl. Phys.*, vol. 122, p. 023103, 2017.
[50] Y. He, R. Yang, H. Zhang, D. Zhou, and G. Wang, "Volume or inside heating thermography using electromagnetic excitation for advanced composite materials," *Int. J. Therm. Sci.*, vol. 111, pp. 41–49, 2017.
[51] A. Mandelis, L. Nicolaides, and Y. Chen, "Structure and the reflectionless/refractionless nature of parabolic diffusion-wave fields," *Phys. Rev. Lett.*, vol. 87, p. 020801, 2001.
[52] F. Vedreno-Santos, M. Riera-Guasp, H. Henao, M. Pineda-Sanchez, and R. Puche-Panadero, "Diagnosis of rotor and stator asymmetries in wound-rotor induction machines under nonstationary operation through the instantaneous frequency," *IEEE Trans. Ind. Electron.*, vol. 61, no. 9, pp. 4947–4959, Sep. 2014.
[53] S. Kaiplavil and A. Mandelis, "Highly depth-resolved chirped pulse photothermal radar for bone diagnostics," *Rev. Sci. Instrum.*, vol. 82, p. 074906, 2011.
[54] S. Kaiplavil, A. Mandelis, X. Wang, and T. Feng, "Photothermal tomography for the functional and structural evaluation, and early mineral loss monitoring in bones," *Biomed. Opt. Exp.*, vol. 5, pp. 2488–2502, Aug. 1, 2014.
[55] S. Kaiplavil, A. Mandelis, and B. T. Amaechi, "Truncated-correlation photothermal coherence tomography of artificially demineralized animal bones: Two- and three-dimensional markers for mineral loss monitoring," *J. Biomed. Opt.*, vol. 19, pp. 026015, Feb. 2014.

Ruizhen Yang (M'16) completed the Joint Ph.D. study in 2012 from the Department of Wood Science, University of British Columbia, Vancouver, BC, Canada, and the School of Civil Engineering, Hunan University, Changsha, China, where she received the Ph.D. degree from the College of Civil Engineering in 2013.

She is an Assistant Professor with Changsha University, Changsha, and a Postdoctoral Fellow with Hunan University. Her current research interests include bamboo wood composite materials, nondestructive testing, and structural health monitoring.

Yunze He (M'11) received the Ph.D. degree in instrument science and technology from National University of Defense Technology, Changsha, China, in 2012, and received the Joint Ph.D. degree in electrical engineering from the School of Electrical, Electronic Engineering, Newcastle University, Newcastle upon Tyne, U.K., and the National University of Defense Technology, China, in 2012.

He is an Assistant Professor in Hunan University, Changsha, China. He has chaired or participated in more than 30 projects including NSFC, EPSRC, etc. He has authore or coauthored more than 50 academic papers in journals, which have been cited more than 1400 times in Google Scholar and the h-index is 22. He has published a book titled *Eddy Current Thermography Non-destructive Testing* in Chinese (National Defense Industry Press, 2012) and a book titled *Transient Electromagnetic-Thermal Nondestructive Testing* in English (Butterworth-Heinemann, 2017). His current research interests include nondestructive testing, condition monitoring, renewable energy, and structural health monitoring.

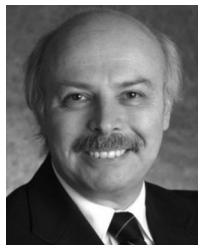

Andreas Mandelis received the Ph.D. degree from the Applied Physics and Materials Laboratory Princeton University, Princeton, NJ, USA, in 1979.

He is a Full Professor of Mechanical and Industrial Engineering and Electrical and Computer Engineering in the Institute of Biomaterials and Biomedical Engineering, University of Toronto, Toronto, ON, Canada. He is also a National 1000-Talents Professor at the University of Electronic Science and Technology of China, Chengdu, China.

He is the Canada Research Chair in Diffusion-Wave and Photoacoustic Sciences and Technologies and Director of the Center for Advanced Diffusion-Wave and Photoacoustic Technologies (CADIPT), University of Toronto. He is the author or coauthor of 400+ scientific papers in refereed journals and 190+ scientific and technical proceedings papers. He is the Editor-in-Chief of the *Springer International Journal of Thermophysics*, an Associate Editor of the *AIP Journals Review of Scientific Instruments*, *Journal of Applied Physics*, Topical Editor of the *OSA Journal Optics Letters*. He is on the Editorial Board of the *SPIE Journal of Biomedical Optics*. He is the Consulting Editor of the AIP flagship magazine *Physics Today*. He has several inventions, 38 patents and patents pending in the areas of photothermal tomographic imaging, signal processing and measurement, nondestructive imaging, hydrogen sensors, dental laser diagnostics (biothermophotonics), infrared photothermal radiometry, laser photo-carrier radiometry, and laser biophotoacoustic tissue imaging.

Nichen Wang is currently working toward the Master's degree at Hunan University, Changsha, China, where he had received the matriculation in 2016.

His current research interests include infrared thermography testing and composite testing in the field of nondestructive testing (NDT) and structural health monitoring (SHM).

Xuan Wu received the Ph.D. degree in automation from Hunan University, Changsha, China, in 2016.

He is a Postdoctoral Fellow with the College of Electrical and Information Engineering, Hunan University. His current research interests include control and testing of permanent magnet machines.

Shoudao Huang (SM'14) received the B.S. and Ph.D. degrees in electrical engineering from the College of Electrical and Information Engineering, Hunan University, Changsha, China, in 1983 and 2005, respectively.

He is currently a Professor with the College of Electrical and Information Engineering, Hunan University. His current research interests include motor design and control, power electronic system and control, and wind energy conversion system.